Making corrections to your proof

Please follow these instructions to mark changes or add notes to your proof. Ensure that you have downloaded the most recent version of Acrobat Reader from **https://get.adobe.com** so you have access to the widest range of annotation tools.

The tools you need to use are contained in **Annotations** in the **Comment** toolbar. You can also right-click on the text for several options. The most useful tools have been highlighted here. If you cannot make the desired change with the tools, please insert a sticky note describing the correction.

Please ensure all changes are visible via the 'Comments List' in the annotated PDF so that your corrections are not missed.

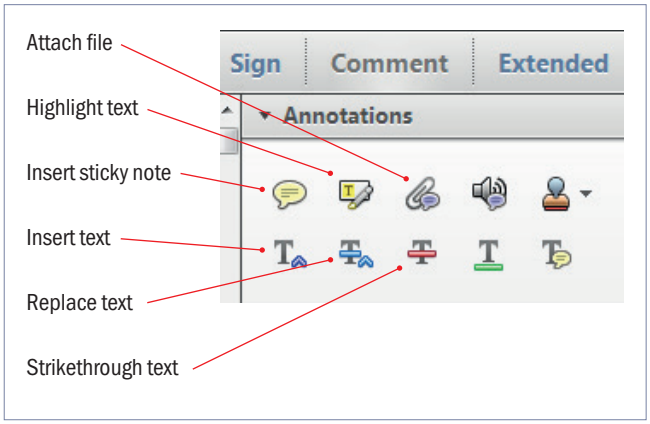

Do not attempt to directly edit the PDF file as changes will not be visible.

Replacing text

To replace text, highlight what you want to change then press the replace text icon, or right-click and press 'Add Note to Replace Text', then insert your text in the pop up box. Highlight the text and right click to style in bold, italic, superscript or subscript.

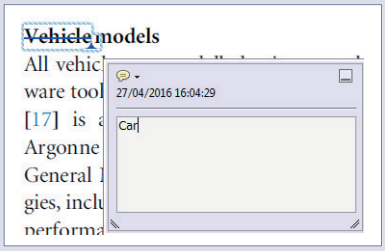

Inserting text

Place your cursor where you want to insert text, then press the insert text icon, or right-click and press 'Insert Text at Cursor', then insert your text in the pop up box. Highlight the text and right click to style in bold, italic, superscript or subscript.

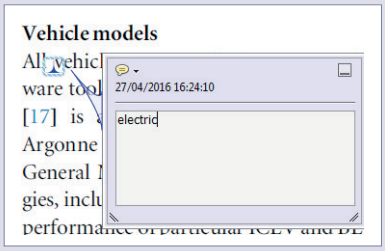

Deleting text

To delete text, highlight what you want to remove then press the strikethrough icon, or right-click and press 'Strikethrough Text'.

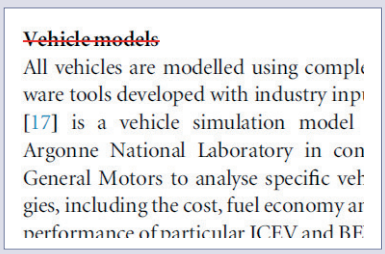

Highlighting text

To highlight text, with the cursor highlight the selected text then press the highlight text icon, or right-click and press 'Highlight text'. If you double click on this highlighted text you can add a comment.

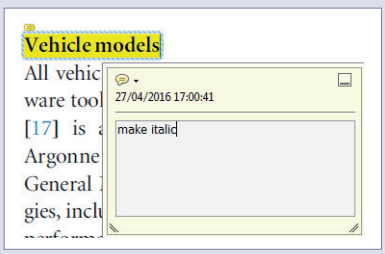

QUERY FORM

JOURNAL: Biofabrication

AUTHOR: J F M Ribeiro *et al*

TITLE: Structural monitoring and modeling of the mechanical deformation of three-dimensional printed poly(ε-caprolactone) scaffolds

ARTICLE ID: bfaa698e

The layout of this article has not yet been finalized. Therefore this proof may contain columns that are not fully balanced/matched or overlapping text in inline equations; these issues will be resolved once the final corrections have been incorporated.

Please check that the names of all authors as displayed in the proof are correct, and that all authors are linked correctly to the appropriate affiliations. Please also confirm that the correct corresponding author has been indicated.

If an explicit acknowledgment of funding is required, please ensure that it is indicated in your article. If you already have an Acknowledgments section, please check that the information there is complete and correct.

We have been provided with ORCID numbers for the authors as below. Please confirm whether the numbers are correct.
Emanuel M Fernandes 0000-0002-4296-2529

Page 12

Q1
Please check the details for any journal references that do not have a link as they may contain some incorrect information. If any journal references do not have a link, please update with correct details and supply a Crossref DOI if available.

Page 13

Q2
Please provide the volume number in reference [29].

APP Template V1.00 Article id: bfaa698e Typesetter: MPS Date received by MPS: 28/03/2017 PE: MAC004070 CE: LE: UNCORRECTED PROOF

IOP Publishing *Biofabrication* **00** (2017) 000000

Biofabrication

RECEIVED
9 November 2016

REVISED
25 March 2017

ACCEPTED FOR PUBLICATION
28 March 2017

PUBLISHED
DD MM 2017

PAPER

Structural monitoring and modeling of the mechanical deformation of three-dimensional printed poly(ε-caprolactone) scaffolds

João F M Ribeiro[1,2], Sara M Oliveira[1,2], José L Alves[3], Adriano J Pedro[1,2], Rui L Reis[1,2], Emanuel M Fernandes[1,2] and João F Mano[1,2,4]

[1] 3B's Research Group—Biomaterials, Biodegradables and Biomimetics, University of Minho, Headquarters of the European Institute of Excellence on Tissue Engineering and Regenerative Medicine, AvePark—Parque de Ciência e Tecnologia, 4805-017 Barco, Guimarães, Portugal
[2] ICVS/3B's-PT Government Associate Laboratory, Braga/Guimarães, Portugal
[3] Center for MicroEletroMechanical Systems Center (CMEMS), University of Minho, Campus de Azurém, 4800-058 Guimarães, Portugal
[4] Present address: CICECO—Aveiro Institute of Materials, Department of Chemistry, University of Aveiro, 3810-193 Aveiro, Portugal.

E-mail: efernandes@dep.uminho.pt

Keywords: poly(ε-caprolactone), 3D printing, additive manufacturing, morphology, mechanical properties, finite element analysis

Supplementary material for this article is available online

Abstract

Three-dimensional (3D) printed poly(ε-caprolactone) (PCL) based scaffolds have being proposed for different tissue engineering applications. This study addresses the design and fabrication of 3D PCL constructs with different struts alignments at 90°, 45° and 90° with offset. The morphology and the mechanical behavior under uniaxial compressive load were assessed at different strain percentages. The combination of a new XtremeCT compression device and micro computed tomography (micro-CT) allowed understanding the influence of pore geometry under controlled compressive strain in the mechanical and structural behavior of PCL constructs. Finite element analysis (FEA) was applied using the micro-CT data to modulate the mechanical response and compare with the conventional uniaxial compression tests. Scanning electron microscopic analysis showed a very high level of reproducibility and a low error comparing with the theoretical values, confirming that the alignment and the dimensional features of the printed struts are reliable. The mechanical tests showed that the 90° architecture presented the highest stiffness. With the XtremeCT device was observed that the 90° and 90° with offset architectures presented similar values of porosity at same strain and similar pore size, contrary to the 45° architecture. Thus, pore geometric configurations affected significantly the deformability of the all PCL scaffolds under compression. The prediction of the FEA showed a good agreement to the conventional mechanical tests revealing the areas more affected under compression load. The methodology proposed in this study using 3D printed scaffolds with Xtreme CT device and FEA is a framework that offers great potential in understanding the mechanical and structural behavior of soft systems for different applications, including for the biomedical engineering field.

1. Introduction

Tissue engineering (TE) procedures often require the use of a porous scaffold, which can be used as a three-dimensional device for initial cell attachment and subsequent tissue formation both *in vitro* and *in vivo* [1]. Scaffold design and fabrication of well-controlled structures and cell instruction functions, are key factors in scaffold-based 3D structures as they dictate their success and eventual application in the medical field. Several techniques have been proposed to fabricate such kind of devices [2, 3]. Considering all the types of available processing techniques, 3D printing is highlighted for allowing layer-by-layer fabrication of 3D scaffolds from computer-assisted designs [4]. Scaffolds can be printed with patient customized-shape, with high cell ingrowth capability, appropriate pore interconnectivity, highly controlled internal geometry and more recently fabricated using bioinks containing cells [5–8]. 3D printing is the ideal tool for creating scaffolds with tuned structural and mechanical properties. Several 3D printing techniques

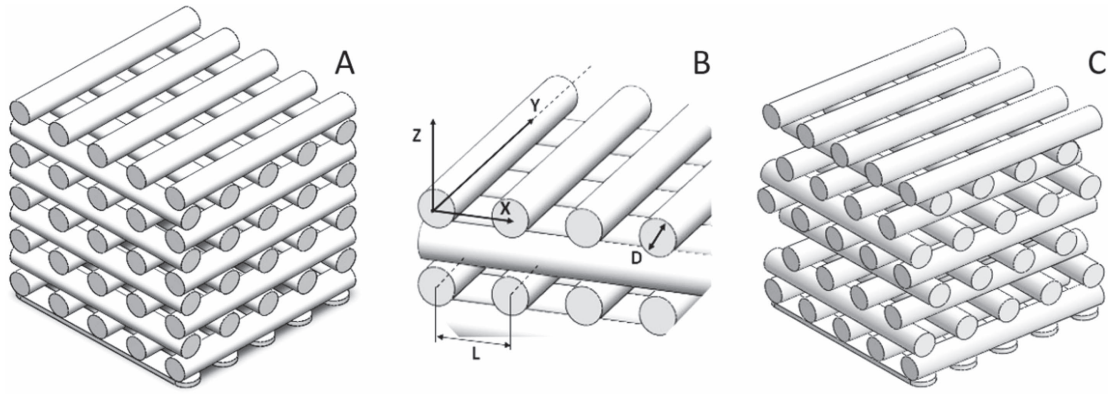

Figure 1. Schemes of the 3D layout of the printed constructs: (A) scaffold design with the subsequent layers aligned by 90°; (B) scaffolds fabricated layer by layer with (L) as strut distance and (D) as fiber diameter; (C) design of the scaffold with alignment of 90° and 0.75 mm of offset (with a strand spacing of 1.5 mm).

have been reported in the biomedical field such as stereolithography [9, 10], selective laser sintering [11, 12], fused deposition modeling [13, 14] and a variety of specific systems for 3D bioprinting [15–17]. Thus, the development of scaffolds that mimic the architecture of tissue is one of the major challenges in the field of TE in the last 15 years [18]. The control of the molecular weight and the configuration of the pore geometry offer great potential for manipulation of mechanical behavior of 3D printed PCL scaffolds [19]. Despite the large amount of work developed that has been reported in the biomedical field [20–22], there is still a lack of knowledge on the behavior of those structures under mechanical compressive load and how that load affects the microarchitecture of the scaffold. When designing a new scaffold, the behavior of the internal structure upon loading should be studied and adequate to the final biomedical application. With this purpose, new devices have been developed, envisioning the dynamic assessment of 3D fracture properties, combining mechanical compression tests and micro computerized tomography imaging (micro-CT), and known as XtremeCT devices. This type of device is characterized for being compatible with non-invasive techniques, being a combination of stepwise microcompression and time-lapsed micro-CT. These devices have precision and accuracy similar to conventional mechanical testing methods. Currently, the main devices found in the literature are: (i) the image-guided failure assessment (IGFA) device —micro-compression device [23]; (ii) the loading device for compression and tension testing design by Hulme PA [24]; (iii) the IGFA device designed by Mueller [25]; (iv) the skyscan material testing stage [26]. Some of the XtremeCT devices allow a continuous deformation simultaneously to the image acquisition, however these systems are expensive and consequently difficult to access. The present study, addresses the design and fabrication of an alternative XtremeCT device for compression tests that could be affordable and simple to use in combination with most of the micro-CTs in order to access and understand the mechanical behavior and structural evolution of scaffolds. The proof of concept of our designed device was demonstrated by evaluating and monitoring morphometric features (porosity and pore size) of 3D printed PCL scaffolds with different struts alignment (90°, 90° with offset and 45°) at different compressive strains (0%, 5%, 15% and 30%). The 3D architectures were evaluated by scanning electron microscopy (SEM), micro-CT and uniaxial mechanical tests.

Finite element approach (FEA) is capable of predicting the mechanical behavior of complex structures like 3D scaffolds if an adequate mesh density is considered [27–29]. Therefore, the study of the effect of the applied load on the structural behavior of the different scaffolds was complemented with a FEA and compared with the conventional uniaxial mechanical tests. The use of effective scaffold assessment techniques is advantageous at the initial stages of research and development to select or design scaffolds with suitable properties for a specific application in the biomedical field. The combination of cost-effective Xtreme CT devices and FEA are expected to contribute more in the understanding and optimization of the behavior of complex 3D structures under mechanical loads.

2. Materials and methods

2.1. Scaffolds design and fabrication

Poly(ε-caprolactone) was bought from Sigma-Aldrich (UK) with an average M_n between 70 000 and 90 000. PCL granules were introduced in a metal cartridge that was further placed in the high temperature head at 160 °C to guarantee the complete polymer melting. Allocated to the head it was used a stainless steel hypodermic needle of 18G to deposit the strands. 3D PCL scaffolds were produced according to three different internal strut orientation (A-90°, B-45° and C-90° with offset) using the 3D Bioplotter™ 4th

generation (EnvisionTEC GmbH, Germany) presented in the scheme of figure 1.

The 3D objects were set with a layer thickness of 640 μm and with a strand spacing of 1.5 mm. The architecture A was produced by the consecutive deposition of 2D layers, in which layer N was plotted orthogonally (performing an angle of 90°) to layer N-1, and was plotted in the same relative position of layer N-2. The architecture B was produced by the consecutive deposition of 2D layers, in which layer N was plotted diagonally (performing an angle of 45°) to layer N-1, and was plotted in the same relative position of layer N-4. The architecture C was similar to A, with exception of layer N being plotted with an offset distance of 0.75 mm relatively to the position of the layer N-2. The selected nozzle comprised a stainless steel needle with an internal diameter of 0.760 mm and a length of 6 mm. Compressed air pressure was set at 5.3 bar and the print speed was 3.6–3.8 mm s^{-1}. The final scaffolds were obtained by cutting with a bistoury the plotted structures into smaller samples ($\cong 5 \times 7 \times 7\ mm^3$), and stored in polyethylene bags at ambient conditions prior to further tests.

2.2. Scaffolds characterization

2.2.1. Scanning electron microscopy (SEM)

The morphological characterization of the PCL scaffolds was performed using high-resolution emission SEM Auriga Compact, Zeiss. The samples were precoated with a conductive layer of sputtered gold in a sputter coater (EM ACE600, Leica). The SEM micrographs were taken at an accelerating voltage of 5.0 and 15.0 kV and at different magnifications.

2.2.2. Mechanical analysis

The mechanical properties of the PCL scaffolds with dimensions ($5 \times 7 \times 7\ mm^3$) were determined using a universal mechanical testing machine INSTRON 5543 under uniaxial compression mode, equipped with a 1 kN load cell, at 1 mm min^{-1}. At least seven samples per condition were tested up to three different strains of 5%, 15% and 30%. In order to diminish the eventual error associated with the specimen dimension, the strength and modulus of each scaffold was normalized by the density of the specimens, as displayed in the following equation (1):

$$\text{Specific Strength or Modulus} = \frac{\text{Compressive (Strength or Modulus)}}{\text{Density}} \times [\text{MPa}/(\text{g cm}^{-3})]. \quad (1)$$

2.2.3. Porosity assessment

2.2.3.1. Theoretical porosity: geometry

The theoretical porosity the 3D printed scaffolds with the 3 above mentioned internal structure was estimated. The equations presented in supplementary information (S1) is available online at stacks.iop.org/BF/0/000000/mmedia consider the contact between the struts of the different layers to be only superficial and the struts to be cylindrical volumes. Therefore, it is expected that the actual porosity can be slightly lower than the one determined theoretically.

2.2.3.2. Indirect porosity: densities

The porosity of the 3D printed PCL scaffolds was evaluated, using the following methodology: (i) measurement of the weight and volume (by measuring the width, length and height) of each sample; (ii) determination of the apparent density of the PCL scaffolds, and (iii) application the following equation:

$$\text{Porosity} = \left(1 - \frac{\rho}{\rho_b}\right) \times 100 \quad (\%), \quad (2)$$

where ρ is the apparent density of the cellular structure (scaffold) and ρ_b is the density of the bulk substance for PCL, $\rho_b = 1.145\ g\ cm^{-3}$, [30, 31].

Seven 3D PCL samples were measured for each group of architecture and for each percentage of strain (%).

2.2.4. XtremeCT device

We developed a device to be combined with micro-CT equipment to study changes in the mechanical properties and structure of the 3D printing PCL scaffolds controlled upon compressive strains as showed in scheme of figure 2. The device comprises a chamber made of poly(methyl methacrylate) that maintains the scaffold under a constant strain (3). It is composed by a small plate made of teflon where it is directly applied the displacement to deform the scaffold (2), and has a conical geometry to avoid the friction and torsion of the scaffold. The load or strain applied to the scaffold is controlled adjusting the rotation angle of the top screw (1).

2.2.5. Micro-computerized tomography

The microstructure of the 3D PCL scaffolds with different internal strut organization (90°, 45° and 90° with offset), loaded and unloaded, was qualitatively and quantitatively evaluated by micro-CT analysis using a Skyscan 1272, Bruker, EUA. Three loaded samples per architecture were previously compressed at different strains of 5%, 15% and 30% in an Instron equipment. The samples were then inserted in the designed XtremeCT device under a constant strain-driven compression, and immediately attached in the micro-CT to perform the standard image acquisition, 2D and 3D analysis. Note that this equipment also allows the direct deformation of the sample by controlling the rotation of the screw. The device is also prepared to include liquids in the chamber under compression. The XtremeCT system was inserted in the micro-CT chamber and the normal technique procedure was performed with a voxel size of 18 μm and image size of 1224×1224 pixels. The x-ray source was 60 kV and 166 μA and a rotation step of

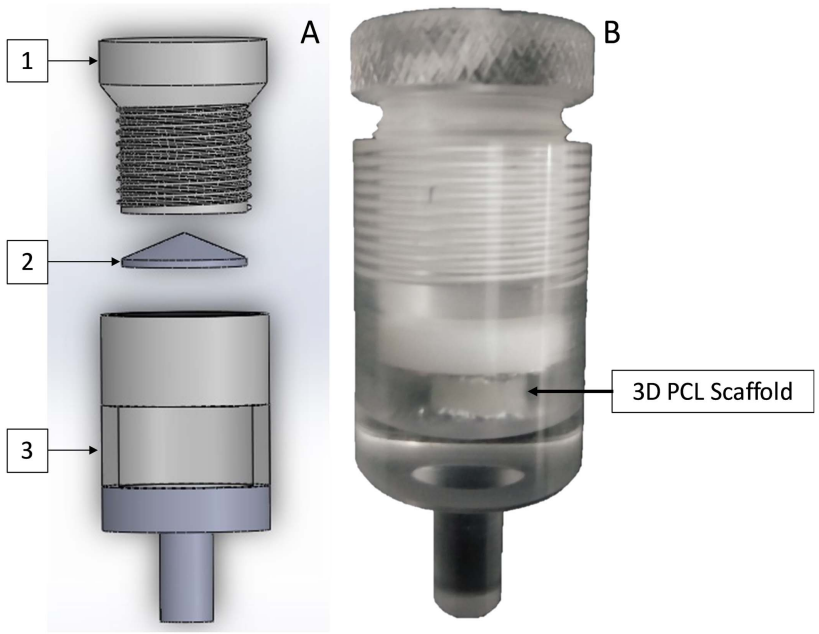

Figure 2. (A) Front view of compressive home-developed XtremeCT device indicating the following elements. 1-screw, 2-conic plate and 3-chamber; (B) photography of the real closed system with the PCL scaffold.

0.6°. The isotropic slice data was obtained by the system and reconstructed into 2D xy slice images. The images were compiled and subsequently render to 3D xyz images to obtain sections of the gray images of the scaffold using NRecon software (v. 1.6.10). The gray images were converted to binary images and the entire scaffold area (including structural pores, but not eventual smaller pores in the struts) was included in the area/volume of interest for the analysis of the morphometric parameters such as pore size, trabecular thickness, porosity of the scaffolds, were analyzed using the CTAn software (v. 1.16).

2.3. Finite element (FE) simulations

This method consisted in creating large-scale FE meshes by directly meshing voxel datasets from micro-CT scans thereby capturing any fabrication feature in the resolution range of the CT scan. The starting Bitmaps images were converted to binary images by segmentation to remove the empty spaces. These images were uploaded into a home-developed software, VCAD, under a research project [32], in order to perform a 3D reconstruction and create 3D voxelised structure, which was then used in the 3D FE mesh generation. The 3D FE mesh generation procedure was based on a two-step algorithm: firstly, and using a home-developed software, vcat2tets, from the 3D voxelised data we generated a very dense and regular four-node tetrahedral FE mesh with good dihedral angles; secondly, the large-scale tetrahedral FE mesh (high density of FE) was then simplified using a second homemade software, simptets. The procedure allowed simplifying the FE mesh by successive edge collapsing until attaining a more reasonable FE mesh size. It is worth mentioning that such procedure preserves the geometric features of the boundaries, as well as the quality of the FE.

2.4. Statistical analysis

The results were presented as a mean ± standard deviation. Statistical analysis was made using one-way and two-way ANOVA followed by Turkey test using Graph-Pad Prism 6.0. Statistical significance is presented as ns: $p > 0.05$, *: $p < 0.05$, **: $p < 0.01$, ***: $p < 0.001$.

3. Results and discussion

3.1. Three dimensional printed PCL scaffolds

We evaluated the effect of struts architecture on both mechanical performance and porosity of the 3D printed scaffolds. Figure 3 shows the SEM micrographs of the three different unloaded architectures 90°, 45°, and 90° with offset, being clear the homogeneity throughout the scaffold. The surface topography of the PCL scaffolds was smooth and the constructs presented a well-defined internal geometry and uniform pore distribution. Similar smooth surfaces and structure, and fully interconnected pore were also reported in other studies [33, 34], using additive manufacturing. A good adhesion was obtained between adjacent layers, as shown in the magnification of the inset micrograph of figure 3 for the top view of the 45° architecture. This behavior was already reported in a previous study [34] using this type of PCL scaffolds, where it was observed the junction between orthogonal fibers.

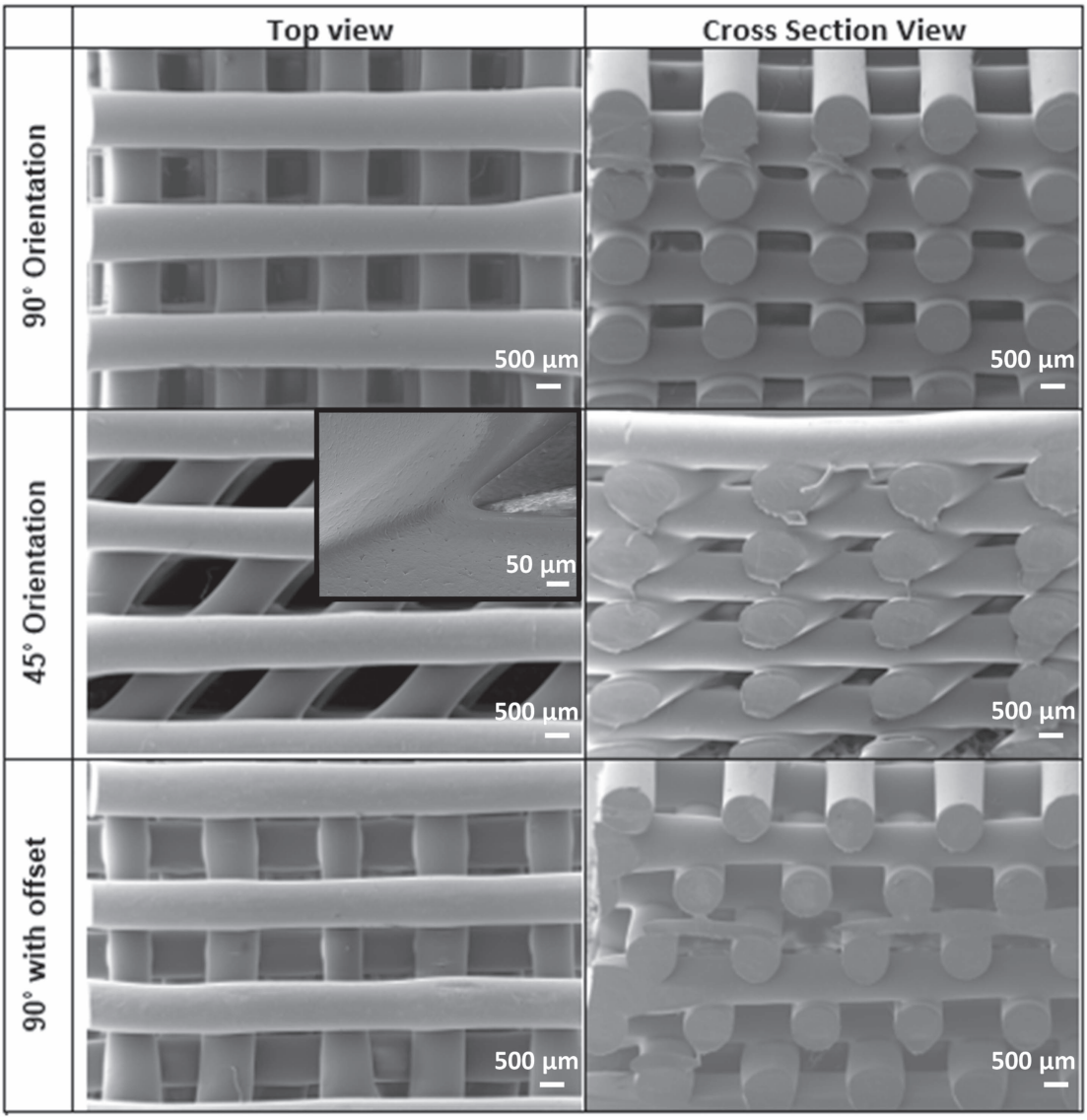

Figure 3. SEM micrographs of the 3D PCL scaffolds fabricated by 3D printing; representation of three different architectures (90°, 45° and 90° with offset) in two different views (top and cross-section).

In order to assess the accuracy of the 3D printing, the fidelity of the struts was determined by comparing the diameter, separation and distance measured by SEM with their respective theoretical ones as depicted in table 1. The theoretical strut diameter was considered the same of the internal nozzle diameter while the remaining others were features defined while programming the layers.

Some deviations on the strut diameter and distance between layers could be detected. Nonetheless, the alignment and the dimensional features of the struts were reliable and showed fidelity between 95.0% up to 99.8% for all PCL scaffolds. In general, this 3D printed PCL scaffolds showed a very high level of fidelity and consequently showed a low error in the final geometry.

3.2. Mechanical properties

The mechanical behavior of the three studied PCL scaffold architectures was experimentally characterized using a uniaxial compression tests. The representative stress–strain curves of the experimental characterization up to a compressive strain of about 60% are displayed on figure 4.

The curves were characterized by the commonly observed [35, 36] initial linear region which suggested an initial elastic response. Then, at 10%–15% of compressive strain, the hardening rate progressively decreased up to around 35%–40% of compressive strain, after which the slope of the curves started to increase again, corresponding to the densification of the scaffold architecture. These results evidenced that the higher compressive modulus and strength was displayed by the 90° architecture scaffold when comparing with the 45° and the offset geometries, being the last the weaker one. The results support the idea that

Table 1. Comparison between the theoretical values defined for PCL scaffold fabrication in 3D printing, and the ones measured by SEM analysis. Data is represented as mean ± SD.

	Strut diameter			Strut separation			Strut distance		
	Theoretical (μm)	SEM (μm)	Fidelity (%)	Theoretical (μm)	SEM (μm)	Fidelity (%)	Theoretical (μm)	SEM (μm)	Fidelity (%)
90°	760	745.0 ± 8.6	98.0	740	741.7	99.8	1500	1486.7	99.1
45°	760	749.7 ± 10.3	98.6	740	702.7	95.0	1500	1452.4	96.8
90° with offset	760	758.1 ± 15.3	99.8	740	713.4	96.4	1500	1471.5	98.1

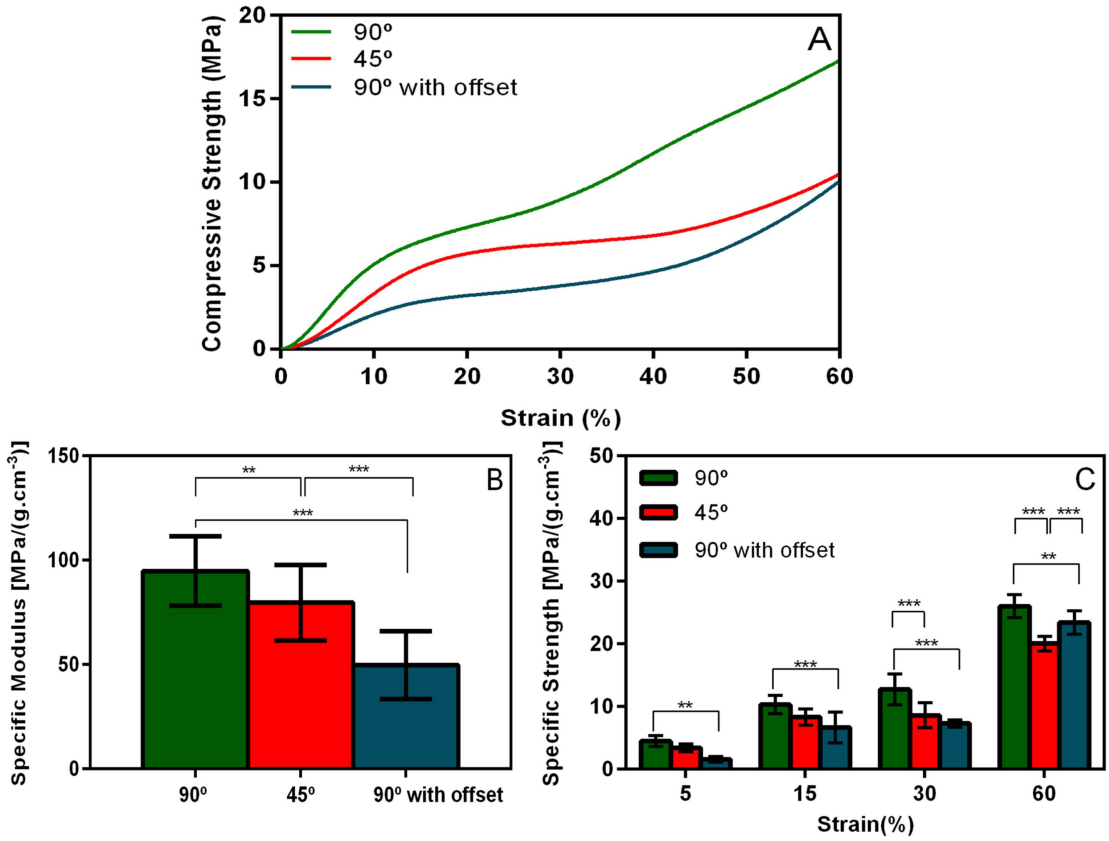

Figure 4. Mechanical behavior of the 3D PCL scaffolds under compression: (A) representative compressive stress–strain curves for each architecture; (B) specific compressive modulus; (C) specific strength in function of strain (%)—for C data is represented as mean ± SD.

varying the geometrical configuration of the 3D architecture changes the mechanical behavior has reported previous works [19, 37].

Taken into account that the material and main filament geometric specifications were the same between scaffolds, any differences in terms of the scaffolds mechanical behavior should be the result on the 3D spatial organization of the filaments on the scaffold. Thus, by playing with the scaffold structure it was possible to adjust considerably the mechanical behavior of the 3D PCL scaffolds under compression. The mechanical properties displayed in figures 4(B) and (C) were obtained by normalizing the compressive modulus and compressive strength with the density of each scaffold. As expected under compression, the specific strength values for each architecture increases with the increasing of the applied strain. The statistical analysis confirmed that the 90° architecture to be slightly higher in terms of specific modulus and specific strength than the other architectures, being in agreement with the representative compressive stress–strain curves.

3.3. Monitoring morphometric features with loading

The major goals of this study were: (i) the development of a micro-mechanical compression device for the in-deep morphometric characterization of unloaded or loaded samples with micro-CT and, simultaneously, (ii) to use this device as a standard tool for studying scaffold failure well beyond the failure region (up to 30% strain). Thus, a new versatile and cost-effective device was designed and tested: see the developed XtremeCT device in figure 2. First, the microstruture of the bare 3D scaffolds was evaluated for their porosity, at an initial stage (0% strain), using three different methods: (i) theoretical calculations; (ii) indirect calculations (using the PCL scaffolds density and the bulk density of PCL); (iii) and by micro-CT analysis. The obtained porosities were in the range of 40% up to 70% as indicated in table 2.

Depending on the fiber orientation within the construct, the porosities of the 3D printed PCL scaffolds were in the range of 50%–70%, similarly to what has been reported by our research group in previous works [6, 38]. As expected, it was observed that the pores were well interconnected throughout the whole structure. The porosity depended on the type of scaffolds and also slightly on the method used for the calculation as indicated in supplementary information (S1). Nonetheless, the total porosity obtained by micro-CT was in accordance to those obtained experimentally and corroborated the results of previous studies [39–41]. However, the theoretical values tended

Table 2. Porosity of the 90°, 90° with offset and 45° 3D PCL scaffolds obtained by theoretical calculation, density and micro-CT analysis (indirect and micro-CT data is presented as mean ± standard deviations).

Architecture	Theoretical (%)	Indirect-density (%)	μCT analysis (%)
90°	55.86	51.63 ± 3.80	45.23 ± 6.13
45°	60.74	48.62 ± 7.05	39.00 ± 4.01
90° with offset	59.38	47.32 ± 3.30	43.78 ± 0.57

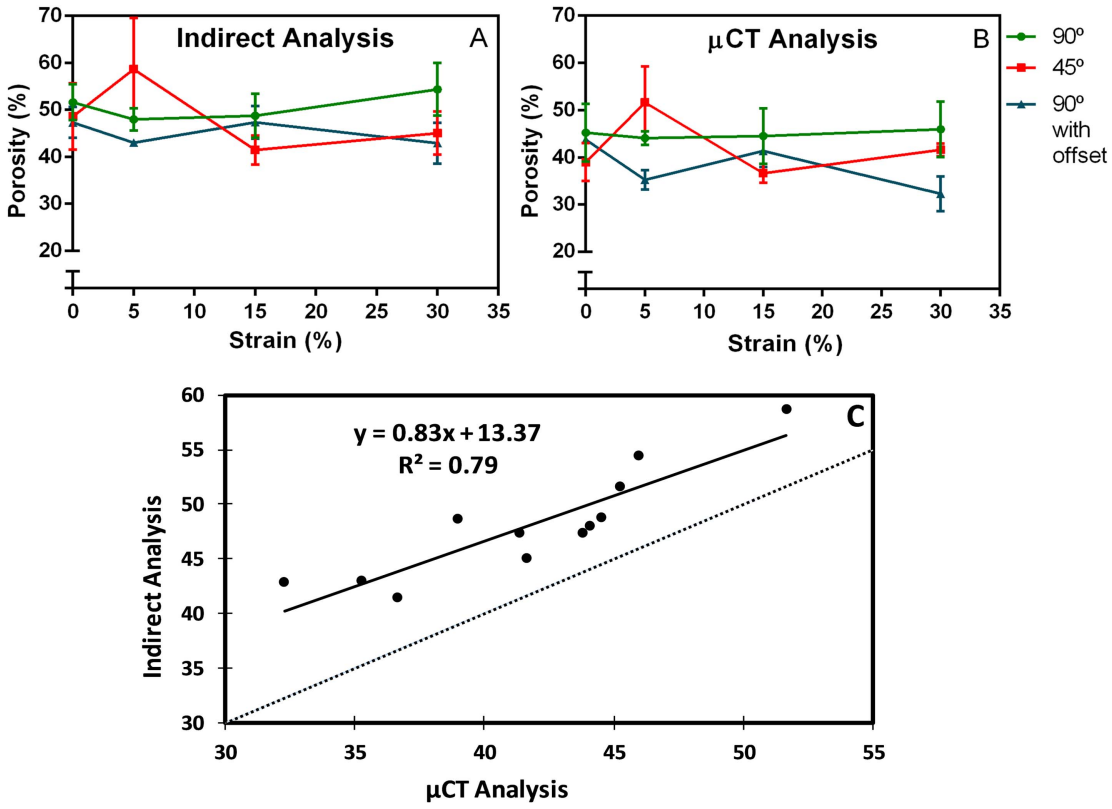

Figure 5. Monitoring of the porosity with the deformation in indirect analysis (A), and micro-CT-XtremeCT analysis (B). (C) Correlation between indirect porosity and porosities measured by micro-CT showing the linear regression line (solid line) and the corresponding fitting parameters. The dashed line shows the expected match between the two types of measurements.

to be little over-estimated. For the calculations, the geometrical features needed to be fixed, such as the fiber diameter and the layer thickness. The fiber diameter was consider to be the same value of the needle internal diameter, however, table 1 shows that they actually tended to be 1%–5% less. Similar trend could be observed to the strut separation. Moreover, some natural and partial overlap occurs between the fibers of subjacent layers during the printing, making the actual layer thickness lower than the theoretical value considered (inner needle diameter). All this small differences have contributed for a slightly over-estimation once the actual volume is lower than the theoretical one.

The morphometric results including porosity and pore size can be seen in figures 5 and 6.

Figures 5(A) and (B) shows that both analysis presented a similar trend even though the Xtreme CT values tend to be slightly lower than the ones obtained from indirect analysis. This monitoring showed that the porosity of the PCL scaffolds behaved differently depending on the internal architecture of the struts. While the 90° showed that between 0% and 30% strain the total porosity was quite stable, the 45° and 90° with offset showed notable shifts. Those two architectures presented distinct behaviors in both analyses, especially at 5% and 15% strain. In the linear region of the compression test at 5% strain, the porosity was higher in the scaffold of 45° and lower in the one of 90° with offset. At 15% strain the opposite shift was observed. At 30% strain, the porosity turned high again in the scaffold 45° and smaller in the scaffold 90° with offset. On the other hand, the scaffolds with a 90° architecture presented a constant behavior over the entire range of applied strains. In this type of scaffold, the pores in the layers were never overlapped with a strut. Therefore, with the scaffold compaction, the pores were not completely closed and the porosity has not significantly changed. It was not possible to see the decrease of porosity because the effect of compression

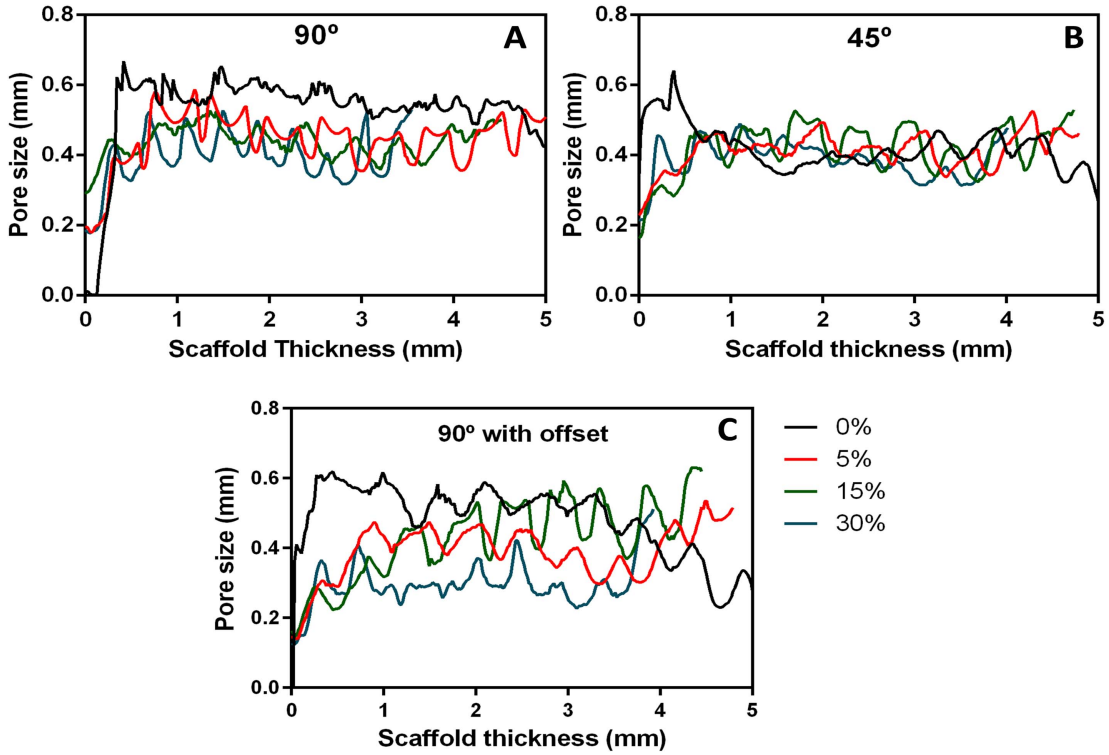

Figure 6. Representative pore size profile with strain variation throughout PCL scaffolds using the XtremeCT device: (A) 90° orientation, (B) 45°orientation and (C) 90°orientation with offset.

only happens from 40% strain as represented in figure 4(A).

Considering the absence of correlation between the compressive modulus and structure thickness in polymer scaffolds described in other studies [39, 40], it was decided to perform a correlation between the indirect and micro-CT porosity. A linear correlation is observed between them and was directly related with a slope of nearly 1, $R^2 = 0.79$ as shown in figure 5(C). The linear regression fit did not cross through the origin, illustrating that the micro-CT porosity is steadily 13% less than the indirect porosity for 3D PCL scaffolds. Based on previous studies reporting 3D scaffolds [34, 42], the observed porosity was consistently between 10% and 30% less than the indirect porosity for porous scaffolds. Considering the dashed line, that shows the expected match between these two types of measurements, the values obtained by indirect analysis were slightly higher than the ones obtained with micro-CT analysis. While porosity can be obtained by indirect methods, as discussed before, any other internal morphometric features of the scaffolds can be monitored without direct observation. Using the XtremeCT device, one could also analyze and monitor *in situ* details along the spatial position with the applied strain, such as, pore size variation with strain, strut thickness variation with strain and porosity variation with scaffold thickness. Figure 6 shows representative curves of the variation of pore size from top to bottom of the unloaded and compressed scaffolds.

The lines in figure 6 showed an expected periodic behavior. The superposition of one layer with the subsequent layer, under strain, should in general lead to a decrease in the pore sizes in the *z* direction and an increase of the pores in the *xy* direction due to the Poisson coefficient effect. Applying higher strain to the scaffolds can induce geometrical changes resulting in different variations of the pore size: (i) packing of the layers (leading to an approximation of the sine-like curves) and consequently increasing the content of struts in the same layer and decreasing pore size, namely: (ii) simultaneous lateral enlargement of the layers hiding the effect of pore size decrease; (iii) non-homogenous sliding of the struts changing the pore size (i.e. above or below).

In all architectures, micro-CT acquisition allowed to achieve a very high-spatial resolution, according to the designed pore sizes, capable of minimizing partial volume effects [43, 44]. The results from the monitoring in figure 6 revealed that the scaffold with the alignment of 90°, with and without offset, presented clear changes in pore size with the increase of strain. The pore size tended to decrease with the increase of deformation. On the other hand, the scaffold with 45° of alignment has not shown noticeable variations in pore size with the strain, despite the effect in the porosity. This suggested that the struts could be sliding much more and the width/length could be increase higher with the deformation much more when printed with the alignment of 45°.

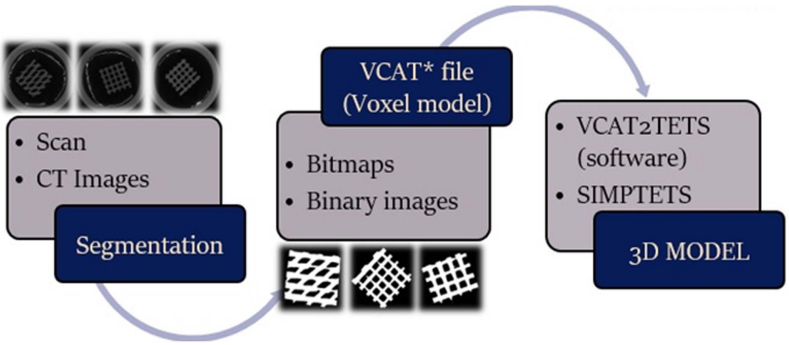

Figure 7. Procedure and software pipeline performed for obtain the final 3D model for FEA: images denoising and segmentation; creation of voxelizd model; and generation, simplification and optimization of 3D FE meshes.

Table 3. Comparison between 3D tetrahedral FE meshes after generation and after simplification, regarding number of nodes and tetrahedral.

	Dense FE mesh		Simplified FE mesh	
Architecture	*Nodes*	*Tetrahedra*	*Nodes*	*Tetrahedra*
90°	442 130	2106 345	155 707	546 462
45°	484 400	2380 712	153 026	549 339
90° with offset	372 197	1772 473	129 591	455 688

3.4. Finite element analysis

The procedure and software pipeline followed to generate the 3D FE models to be used in finite element analysis is schematically described in figure 7.

The used approach followed a logical order, i.e.: (i) denoising, smoothing and segmentation of the micro-CT images; (ii) domain 3D reconstruction: voxelized data; (iii) 3D FE mesh generation: vcat2tets—from 3D voxelized data to a very dense tetrahedral FE mesh; (iv) 3D FE mesh simplification and optimization: simptets —simplification of the initially dense tetrahedral FE mesh (a brief summary of the sizes—number of nodes and number of tetrahedral—of the final FE meshes is shown in table 3); and (v) optimization and artifacts removal of the final 3D FE mesh for finite element analysis.

Considering the 3D FE meshes displayed at 15% compressive strain, shown on the 3rd column of figure 8, where are displayed the isovalues of the von Mises equivalent stress, it was observed that the range of those isovalues were comprised between 0 and 30 MPa. Besides, it was also clear the non-uniformity of the equivalent stress field throughout the scaffolds. Other deformed FE meshes for different levels of compressive strains, presented in supplementary information (S2), displayed higher effect of the compressive load response for higher strains. Regarding the color spectrum, it was observed that the 45° architecture were the structure more affected, resulting in layers under higher strains. Thus, this architecture denoted higher stresses under compressive load in comparison with the other two scaffold geometries, in accordance with experimental mechanical results.

3.5. Comparison of experimental and numerical results

Numerical simulations of the uniaxial compressive loading test were carried out with a fully implicit elastoplastic home-developed FE solver [45]. The PCL material was assumed to behave linear elastic and fully isotropic. The PCLs elastoplastic mechanical properties adopted on the numerical simulations were: (i) Young's modulus = 307.5 MPa; (ii) Poisson ratio = 0.3; (iii) yield strength = 11.4 MPa; and (iv) ultimate strength = 38.7 MPa. Such values of the mechanical properties are bulk properties taken from the literature [46, 47]. All numerical simulations were carried out with the tetrahedral FE meshes previously described. Boundary conditions were imposed in order to mimic the experimental setup.

Contact with low friction (due to teflon) was considered between the sample and the tools numerically modeled by Nagata patches, with a friction coefficient of 0.05 [48]. Figure 9 shows a comparison between experimental and numerical results of the uniaxial compressive loading tests for each scaffold architecture. Good agreement was observed between experimental and numerical results in the case of 90° and 90° with offset scaffolds, mostly in elastic regime. Comparing the present work with other reported studies [39, 46, 47, 49], this approach was considered reliable since similar results using 90° and 90° with offset 3D scaffolds were accomplished as shown in figures 9(A), (C). On the other hand, for the 45° architecture scaffolds, the numerical results slightly over predicted the experimental ones.

However, the FE model still predicted a curve with a similar behavior, i.e., there was a clear elastic region with higher modulus and, after, a plastic behavior region where full recovery of the architecture was irreversible as indicated in figure 9(B). For better comprehension and validation, the compressive modulus was calculated, given that they provide a better and more objective comparison between experimental and numerical results.

Thus, comparing experimentally and numerically compressive modulus showed the three architectures

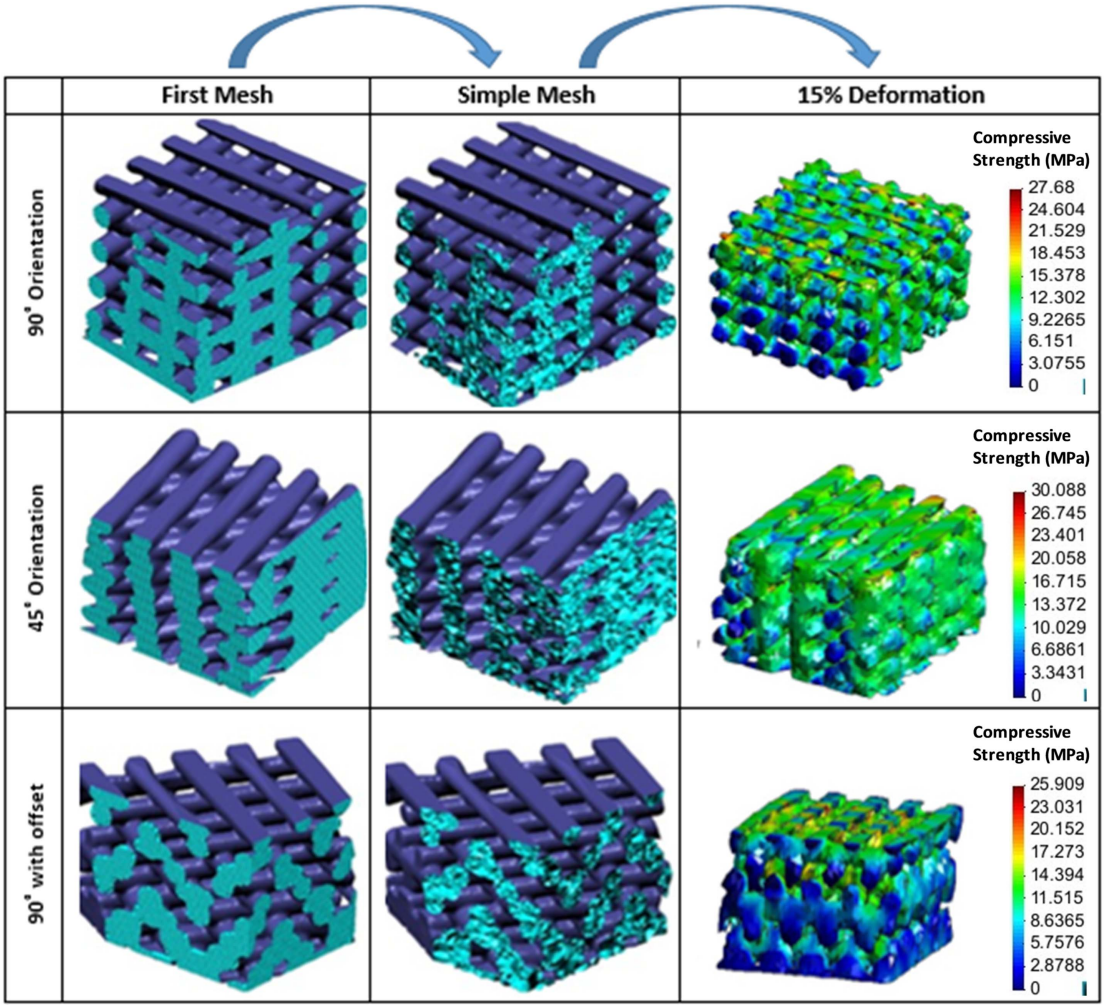

Figure 8. Initial very dense FE meshes (1st column), simplified FE meshes (2nd column) and deformed FE meshes corresponding to 15% of compressive strain (3rd column), for the three struts studied: 90°, 45° and 90° with offset scaffolds.

to be quite similar as presented in figure 9(D). The results clearly showed that this approach can be successfully used to determine the scaffolds mechanical performance before physical testing, supporting the design and advanced analysis.

4. Conclusions

This study presents a new device for a controlled evaluation of the local displacements, strains and porosities in 3D printed scaffolds with different architectures considering all the detail information obtained in two new methodologies: (i) mechanical tests combine with micro-CT analysis (XtremeCT device); (ii) and micro-CT analysis combine with finite element analysis. The PCL scaffolds fabricated via 3D printing possessed appropriated mechanical properties suggesting that they may have the ability of withstand early functional loading in biomedical applications. Between the 3 architectures investigated, we concluded, that the 90° architecture presented higher stiffness under uniaxial compression load. SEM analysis confirmed the fidelity of produced 3D PCL scaffolds with Biolplotter^{TM}. XtremeCT device allowed to study the porosity and other morphometric features of PCL scaffolds with three different architectures at different strains (5%, 15% and 30%). The 90° and 90° with offset scaffolds showed similar values of porosity (%) and pore size at different strain (%), while, the 45° orientation has varied. FEA was successfully applied to predict the mechanical behavior of the 3D PCL scaffolds with different internal structures. The mechanical properties were predictable in most of the cases, and the areas more affected by the compression load could be clearly visualized. Simple devices such as the developed XtremeCT combined with finite element methods are an effective approach allowing the study, optimization and understanding of the mechanical behavior of the scaffolds with different internal geometry. Such tools could be effective in designing optimized porous scaffolds to be used in tissue engineering applications.

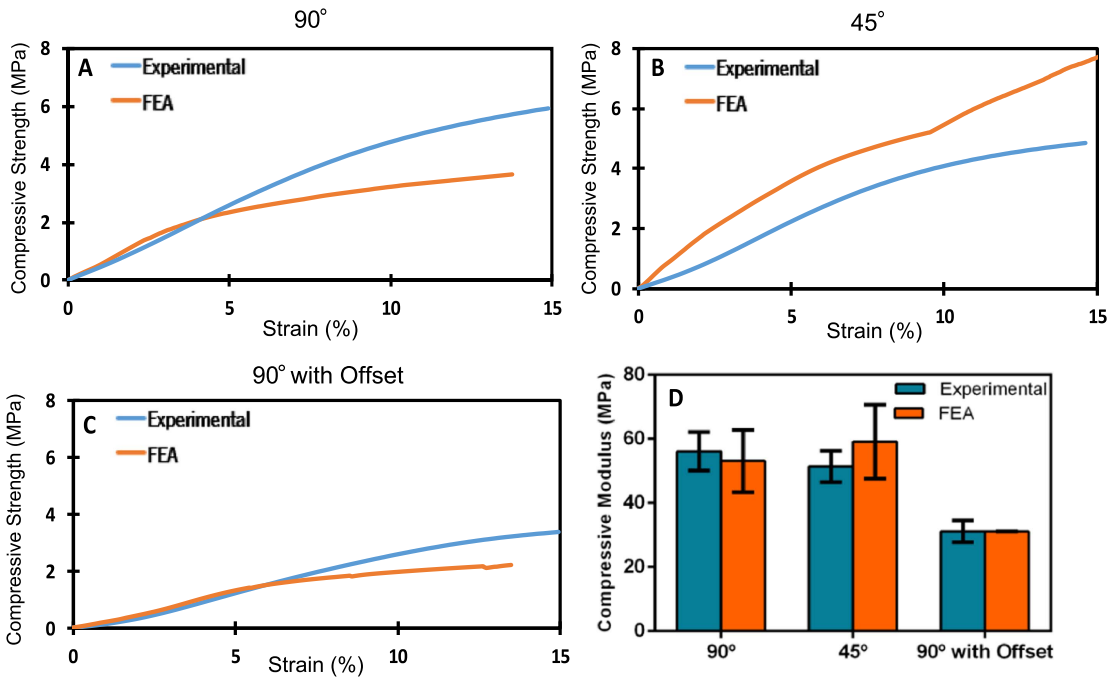

Figure 9. Comparison between the results obtained from mechanical compression tests of 3D PCL scaffolds and the finite element simulations: (A) 90° architecture, (B) 45° architecture, (C) 90°with offset architecture and (D) Young's modulus of the three different architectures.

Acknowledgments

The author Fernandes E M acknowledges the financial support from the Portuguese Foundation for Science and Technology (FCT) and 'Programa Operacional Potencial Humano—POPH' and 'Fundo Social Europeu—FSE' for the post-doctoral grant (SFRH/BPD/96197/2013).

References

[1] Holzapfel B M *et al* 2015 Tissue engineered humanized bone supports human hematopoiesis *in vivo Biomaterials* **61** 103–14
[2] Hutmacher D W 2001 Scaffold design and fabrication technologies for engineering tissues-state of the art and future perspectives *J. Biomater. Sci. Polym. Ed.* **12** 107–24
[3] Kolewe M E, Park H, Gray C, Ye X, Langer R and Freed L E 2013 3D structural patterns in scalable, elastomeric scaffolds guide engineered tissue architecture *Adv. Mater.* **25** 4459–65
[4] Oliveira S M, Reis R L and Mano J F 2015 Towards the design of 3D multiscale instructive tissue engineering constructs: current approaches and trends *Biotechnol. Adv.* **33** 842–55
[5] Park S H, Park D S, Shin J W, Kang Y G, Kim H K, Yoon T R and Shin J W 2012 Scaffolds for bone tissue engineering fabricated from two different materials by the rapid prototyping technique: PCL versus PLGA *J. Mater. Sci., Mater. Med.* **23** 2671–8
[6] Yilgor P, Sousa R A, Reis R L, Hasirci N and Hasirci V 2008 3D plotted PCL scaffolds for stem cell based bone tissue engineering *Macromol. Symp.* **269** 92–9
[7] Murphy S V and Atala A 2014 3D bioprinting of tissues and organs *Nat. Biotechnol.* **32** 773–85
[8] Giannitelli S M, Accoto D, Trombetta M and Rainer A 2014 Current trends in the design of scaffolds for computer-aided tissue engineering *Acta Biomater.* **10** 580–94
[9] Cooke M N, Fisher J P, Dean D, Rimnac C and Mikos A G 2003 Use of stereolithography to manufacture critical-sized 3D biodegradable scaffolds for bone ingrowth *J. Biomed. Mater. Res.* B **64** 65–9
[10] Kwon I K and Matsuda T 2005 Photo-polymerized microarchitectural constructs prepared by microstereolithography using liquid acrylate-end-capped trimethylene carbonate-based prepolymers *Biomaterials* **26** 1675–84
[11] Leong K F, Phua K K S, Chua C K, Du Z H and Teo K O M 2001 Fabrication of porous polymeric matrix drug delivery devices using the selective laser sintering technique *Proc. Inst. Mech. Eng.* H **215** 191–2
[12] Low K H, Leong K F, Chua C K, Du Z H and Cheah C M 2001 Characterization of SLS parts for drug delivery devices *Rapid Prototyping J.* **7** 262–8
[13] Leong K F, Cheah C M and Chua C K 2003 Solid freeform fabrication of three-dimensional scaffolds for engineering replacement tissues and organs *Biomaterials* **24** 2363–78
[14] Zein I, Hutmacher D W, Tan K C and Teoh S H 2002 Fused deposition modeling of novel scaffold architectures for tissue engineering applications *Biomaterials* **23** 1169–85
[15] Landers R, Pfister A, Hübner U, John H, Schmelzeisen R and Mülhaupt R 2002 Fabrication of soft tissue engineering scaffolds by means of rapid prototyping techniques *J. Mater. Sci.* **37** 3107–16
[16] Landers R, Hübner U, Schmelzeisen R and Mülhaupt R 2002 Rapid prototyping of scaffolds derived from thermoreversible hydrogels and tailored for applications in tissue engineering *Biomaterials* **23** 4437–47
[17] Wong J Y, Velasco A, Rajagopalan P and Pham Q 2003 Directed movement of vascular smooth muscle cells on gradient-compliant hydrogels *Langmuir* **19** 1908–13
[18] Fernandes E M, Pires R A, Mano J F and Reis R L 2013 Bionanocomposites from lignocellulosic resources: properties, applications and future trends for their use in the biomedical field *Prog. Polym. Sci.* **38** 1415–41
[19] Olubamiji A D, Izadifar Z, Si J L, Cooper D M L, Eames B F and Chen D X 2016 Modulating mechanical behaviour of 3D-printed cartilage-mimetic PCL scaffolds: influence of molecular weight and pore geometry *Biofabrication* **8** 25020

[20] Canha-Gouveia A, Rita Costa-Pinto A, Martins A M, Silva N A, Faria S, Sousa R A, Salgado A J, Sousa N, Reis R L and Neves N M 2015 Hierarchical scaffolds enhance osteogenic differentiation of human Wharton's jelly derived stem cells *Biofabrication* **7** 35009
[21] Jung J W, Lee H, Hong J M, Park J H, Shim J H, Choi T H and Cho D-W 2015 A new method of fabricating a blend scaffold using an indirect three-dimensional printing technique *Biofabrication* **7** 45003
[22] Qi X, Huang Y, Han D, Zhang J, Cao J, Jin X, Huang J, Li X and Wang T 2016 Three-dimensional poly (ε-caprolactone)/ hydroxyapatite/collagen scaffolds incorporating bone marrow mesenchymal stem cells for the repair of bone defects *Biomed. Mater.* **11** 25005
[23] Nazarian A and Müller R 2004 Time-lapsed microstructural imaging of bone failure behavior *J. Biomech.* **37** 55–65
[24] Hulme P A, Boyd S K, Heini P F and Ferguson S J 2009 Differences in endplate deformation of the adjacent and augmented vertebra following cement augmentation *Eur. Spine. J.* **18** 614–23
[25] Mueller T L, Basler S E, Müller R and Van Lenthe G H 2013 Time-lapsed imaging of implant fixation failure in human femoral heads *Med. Eng. Phys.* **35** 636–43
[26] Tsafnat N and Wroe S 2011 An experimentally validated micromechanical model of a rat vertebra under compressive loading *J. Anat.* **218** 40–6
[27] Zannoni C, Mantovani R and Viceconti M 1999 Material properties assignment to finite element models of bone structures: a new method *Med. Eng. Phys.* **20** 735–40
[28] Hsu J T, Chang C H, Huang H L, Zobitz M E, Chen W P, Lai K A and An K N 2007 The number of screws, bone quality, and friction coefficient affect acetabular cup stability *Med. Eng. Phys.* **29** 1089–95
[29] Alberich-Bayarri A, Sánchez M, Pérez M and Moratal D 2010 Microfinite element modelling for evaluating polymer scaffolds architecture and their mechanical properties from *Finite Elem. Anal.* 251–65
[30] Domingos M, Dinucci D, Cometa S, Alderighi M, Bártolo P J and Chiellini F 2009 Polycaprolactone scaffolds fabricated via bioextrusion for tissue engineering applications *Int. J. Biomater.* **2009** 1–9
[31] Mohanty S, Sanger K, Heiskanen A, Trifol J, Szabo P, Dufva M, Emnéus J and Wolff A 2016 Fabrication of scalable tissue engineering scaffolds with dual-pore microarchitecture by combining 3D printing and particle leaching *Mater. Sci. Eng.* C **61** 180–9
[32] VCAD System Research Program 2010 Retrieved from (https://vcad-hpsv.riken.jp/en/release_software/block/01.php)
[33] Moroni L, de Wijn J R and van Blitterswijk C A 2006 3D fiber-deposited scaffolds for tissue engineering: influence of pores geometry and architecture on dynamic mechanical properties *Biomaterials* **27** 974–85
[34] Sobral J M, Caridade S G, Sousa R A, Mano J F and Reis R L 2011 Three-dimensional plotted scaffolds with controlled pore size gradients: effect of scaffold geometry on mechanical performance and cell seeding efficiency *Acta Biomater.* **7** 1009–18
[35] Vikingsson L, Claessens B, Gómez-Tejedor J A, Gallego Ferrer G and Gómez Ribelles J L 2015 Relationship between micro-porosity, water permeability and mechanical behavior in scaffolds for cartilage engineering *J. Mech. Behav. Biomed. Mater.* **48** 60–9
[36] Patrício T, Domingos M, Gloria A, D'Amora U, Coelho J F and Bártolo P J 2014 Fabrication and characterisation of PCL and PCL/PLA scaffolds for tissue engineering *Rapid Prototyping J.* **20** 145–56
[37] Gloria A, Causa F, Russo T, Battista E, Della Moglie R, Zeppetelli S, De Santis R, Netti P A and Ambrosio L 2012 Three-dimensional poly(ε-caprolactone) bioactive scaffolds with controlled structural and surface properties *Biomacromolecules* **13** 3510–21
[38] Oliveira S M, Silva T H, Reis R L and Mano J F 2013 Hierarchical fibrillar scaffolds obtained by non-conventional layer-by-layer electrostatic self-assembly *Adv. Healthcare Mater.* **2** 422–7
[39] Alberich-Bayarri A *et al* 2009 Microcomputed tomography and microfinite element modeling for evaluating polymer scaffolds architecture and their mechanical properties *J. Biomed. Mater. Res.* B **91** 191–202
[40] Lin A S P, Barrows T H, Cartmell S H and Guldberg R E 2003 Microarchitectural and mechanical characterization of oriented porous polymer scaffolds *Biomaterials* **24** 481–9
[41] Hoque M E, San W Y, Wei F, Li S, Huang M-H, Vert M and Hutmacher D W 2009 Processing of polycaprolactone and polycaprolactone-based copolymers into 3D scaffolds, and their cellular responses *Tissue Eng.* A **15** 3013–24
[42] Williams J M, Adewunmi A, Schek R M, Flanagan C L, Krebsbach P H, Feinberg S E, Hollister S J and Das S 2005 Bone tissue engineering using polycaprolactone scaffolds fabricated via selective laser sintering *Biomaterials* **26** 4817–27
[43] Adachi T, Tsubota K, Tomita Y and Hollister S J 2001 Trabecular surface remodeling simulation for cancellous bone using microstructural voxel finite element models *J. Biomech. Eng.* **123** 403–9
[44] Nagaraja S, Couse T L and Guldberg R E 2005 Trabecular bone microdamage and microstructural stresses under uniaxial compression *J. Biomech.* **38** 707–16
[45] Menezes L F, Neto D M, Oliveira M C and Alves J L 2011 Improving computational performance through HPC techniques: case study using DD3IMP in-house code *AIP Conf. Proc.* **1353** 1220–5
[46] Eshraghi S and Das S 2012 Micromechanical finite-element modeling and experimental characterization of the compressive mechanical properties of polycaprolactone-hydroxyapatite composite scaffolds prepared by selective laser sintering for bone tissue engineering *Acta Biomater.* **8** 3138–43
[47] Eshraghi S and Das S 2010 Mechanical and microstructural properties of polycaprolactone scaffolds with one-dimensional, two-dimensional, and three-dimensional orthogonally oriented porous architectures produced by selective laser sintering *Acta Biomater.* **6** 2467–76
[48] Neto D M, Oliveira M C, Menezes L F and Alves J L 2013 Nagata patch interpolation using surface normal vectors evaluated from the IGES file *Finite Elem. Anal. Des.* **72** 35–46
[49] Diego R B, Estellés J M, Sanz J A, García-Aznar J M and Sánchez M S 2007 Polymer scaffolds with interconnected spherical pores and controlled architecture for tissue engineering: fabrication, mechanical properties, and finite element modeling *J. Biomed. Mater. Res.* B **81B** 448–55

Q2